Since January 2020 Elsevier has created a COVID-19 resource centre with free information in English and Mandarin on the novel coronavirus COVID-19. The COVID-19 resource centre is hosted on Elsevier Connect, the company's public news and information website.

Biosensors and Bioelectronics 213 (2022) 114459

Contents lists available at ScienceDirect

Biosensors and Bioelectronics

journal homepage: www.elsevier.com/locate/bios

A compact, low-cost, and binary sensing (BiSense) platform for noise-free and self-validated impedimetric detection of COVID-19 infected patients

Razieh Salahandish [a,b], Pezhman Jalali [a], Hamed Osouli Tabrizi [c], Jae Eun Hyun [d], Fatemeh Haghayegh [a], Mahmood Khalghollah [a,e], Azam Zare [a], Byron M. Berenger [f,g], Yan Dong Niu [d,**], Ebrahim Ghafar-Zadeh [c,***], Amir Sanati-Nezhad [a,b,h,*]

[a] BioMEMS and Bioinspired Microfluidic Laboratory, Department of Biomedical Engineering, University of Calgary, Calgary, Alberta, T2N 1N4, Canada
[b] Department of Mechanical and Manufacturing Engineering, University of Calgary, University of Calgary, Calgary, Alberta, T2N 1N4, Canada
[c] Biologically Inspired Sensors and Actuators (BioSA), Department of Electrical Engineering and Computer Science, Lassonde School of Engineering, York University, Toronto, M3J1P3, Canada
[d] Department of Ecosystem and Public Health, Faculty of Veterinary Medicine, University of Calgary, Calgary, Alberta, T2N 1N4, Canada
[e] Department of Electrical and Software Engineering, University of Calgary, Calgary, Alberta, T2N 1N4, Canada
[f] Department of Pathology and Laboratory Medicine, University of Calgary, 3535 Research Rd. Calgary, Alberta, T2L 1Y1, Canada
[g] Alberta Public Health Laboratory, Alberta Precision Laboratories, 3330 Hospital Drive, Calgary, Alberta, T2N 4W4, Canada
[h] Biomedical Engineering Graduate Program, University of Calgary, Calgary, Alberta, T2N 1N4, Canada

ARTICLE INFO

Keywords:
SARS-CoV-2
Electrochemical biosensing
Bi-potentiostat
Point-of-care
Rapid tests

ABSTRACT

Electrochemical immuno-biosensors are one of the most promising approaches for accurate, rapid, and quantitative detection of protein biomarkers. The two-working electrode strip is employed for creating a self-supporting system, as a tool for self-validating the acquired results for added reliability. However, the realization of multiplex electrochemical point-of-care testing (ME-POCT) requires advancement in portable, rapid reading, easy-to-use, and low-cost multichannel potentiostat readers. The combined multiplex biosensor strips and multichannel readers allow for suppressing the possible complex matrix effect or ultra-sensitive detection of different protein biomarkers. Herein, a handheld binary-sensing (BiSense) bi-potentiostat was developed to perform electrochemical impedance spectroscopy (EIS)-based signal acquisition from a custom-designed dual-working-electrode immuno-biosensor. BiSense employs a commercially available microcontroller and out-of-shelf components, offering the cheapest yet accurate and reliable time-domain impedance analyzer. A specific electrical board design was developed and customized for impedance signal analysis of SARS-CoV-2 nucleocapsid (N)-protein biosensor in spiked samples and alpha variant clinical nasopharyngeal (NP) swab samples. BiSense showed limit-of-detection (LoD) down to 56 fg/mL for working electrode 1 (WE1) and 68 fg/mL for WE2 and reported with a dynamic detection range of 1 pg/mL to 10 ng/mL for detection of N-protein in spiked samples. The dual biosensing of N-protein in this work was used as a self-validation of the biosensor. The low-cost (~USD $40) BiSense bi-potentiostat combined with the immuno-biosensors successfully detected COVID-19 infected patients in less than 10 min, with the BiSense reading period shorter than 1.5 min, demonstrating its potential for the realization of ME-POCTs for rapid and hand-held diagnosis of infections.

1. Introduction

Label-free, accurate, quantitative, and low-cost electrochemical immuno-biosensors are one of the most promising approaches for accurate, rapid, and quantitative detection of various bodily fluid proteins, cytokines, and hormones. These biosensors have been used for the early diagnosis of several diseases, such as brain injuries (Khetani et al. 2018, 2021), cancer (Akhavan et al., 2014; Chung et al., 2021; Pimalai

* Corresponding author. BioMEMS and Bioinspired Microfluidic Laboratory, Department of Biomedical Engineering, University of Calgary, Calgary, Alberta, T2N 1N4, Canada.
** Corresponding author.
*** Corresponding author.
E-mail addresses: dongyan.niu@ucalgary.ca (Y.D. Niu), egz@cse.yorku.ca (E. Ghafar-Zadeh), amir.sanatinezhad@ucalgary.ca (A. Sanati-Nezhad).

https://doi.org/10.1016/j.bios.2022.114459
Received 4 May 2022; Accepted 6 June 2022
Available online 14 June 2022

et al., 2021), infectious diseases (Idili et al., 2021; Wu et al., 2018), and other clinical and pharmaceutical applications (Arduini et al., 2016; Castle et al., 2021; El Harrad et al., 2018; Monošík et al., 2012). For complex bodily fluids such as the blood, the matrix effect has been a critical challenge for the reliable detection of several biomarkers for which multiplex biosensors with the capability of detecting matrix effect are highly beneficial (Gao et al., 2017; Liu et al., 2021; Salahandish et al., 2022a; Timilsina et al., 2021; Zupančič et al., 2021). The use of multiple electrodes (Panes-Ruiz et al., 2021) in the format of electrode arrays has been also investigated as a self-validation mechanism for avoiding false-positive results, relying on the fact that the results from each electrode were comparable. In self-varified systems that use two different detection mechanisms, e.g. optical and electrochemical, two working electrode designs have been exploited to add to the reliability of the results in case of need or act as a self-supporting tool (Ibarlucea et al., 2016).

Multiplex electrochemical point-of-care testing (ME-POCT) devices are expected to have four major compartments: 1) reliable and reproducible electrodes created using inkjet or screen printing methods, 2) an accurate biosensing protocol for mediating the electrode surface to create accurate biosensors, 3) microfluidics for automating electrochemical biosensing steps, and 4) and an accurate and low-cost multichannel potentiostat with an easy-to-use interface for data interpretation and wireless data transfer. Despite enormous advances in developing multiplex screen printed electrodes and electrochemical biosensors (Dhanapala et al., 2020; Khetani et al., 2019; Kinnamon et al., 2018; Noah and Ndangili, 2019; Salahandish et al. 2019, 2022a) as well as the recent progress in self-powered microfluidic devices (Haghayegh et al. 2022a, 2022b; Nyein et al., 2018; Salahandish et al., 2022b), the realization of ME-POCT requires the development of new hand-held, rapid and remote reading, easy-to-use, noise-free, and cheaper multichannel potentiostat readers (Alam et al., 2020; Bianchi et al., 2021).

Several researchers have attempted to develop new multichannel potentiostats, but they are neither low-cost enough to be used for low-cost POCT (e.g., for detection of COVID-19 outside of a laboratory) nor sensitive and noise-free enough to meet the high sensitivity needs of ultrasensitive electrochemical biosensors (Alam et al., 2021; Park et al., 2022; Ramfos et al., 2013; Vinoth et al., 2021; Wu et al., 2018). The output signals of these readers whether square wave, cyclic voltammetry, or impedance (Pellitero et al., 2021), deals with curve-shaped data that needs further data analysis and curve-fitting approaches to obtain the biosensor data, adding to the complexity of the reader (Abdullah et al., 2019; Bianchi et al., 2019; Hoilett et al., 2020; Pruna et al., 2018; Wu et al., 2018). Our multiplex μDrop reader with the capability of simultaneous detection of 1–8 proteins and with comparable performance to the commercial readers was promising toward realizing ME-POCT of panel biomarkers (Khetani et al., 2021). However, rapid testing of diseases using ME-POCTs needs much cheaper readers than μDrop (~$1500).

More importantly, many multichannel potentiostats record electrochemical signals from multiple electrodes one after another in a sequential manner (Clark et al., 2021; Pansodtee et al., 2021; Ramfos et al., 2013; Stradolini et al., 2016; Wu et al., 2018). However, the interaction of the electrodes with the biosample and the redox reagent is highly dynamic and frequency-dependent (Massey et al., 2021; Pothipor et al., 2021). To reach accurate signals from each of the electrodes, particularly when using accurate but slow electrochemical impedance spectroscopy (EIS) reading module (Capaldo et al., 2016), the signals need to be recorded at each testing frequency for all working electrodes prior to reading the response in the subsequent testing frequency. In our recent bipotentiostat design (Bi-ECDAQ), we addressed this concern via a parallel signal reading of two biosensors simultaneously wherein the reader showed an improved response compared to the expensive commercial potentiostat (Salahandish et al., 2022a). However, further advances are required to cancel noises, improve signal acquisition and interpretation, increase the accuracy of curve fitting, reduce the cost, and enable remote control and access, all needed for the realization of ME-POCT.

This work presents a new handheld binary-sensing (BiSense) bipotentiostat to perform EIS-based signal acquisition from a custom-designed dual working electrode immuno-biosensor created using a ready-to-immobilize antibody method. BiSense employs a commercially available microcontroller and out-of-shelf components, offering the cheapest (<USD $40) yet accurate and reliable time-domain impedance analyzer. BiSense offers features such as a noise cancellation system, improved interface, least-square curve fitting, and remote control and access, which adds to its superiority in EIS sensing, the feasibility of use, user-friendliness, and ability to rapidly share the results with users and physicians. This reader can also operate autonomously without the need for other devices (e.g., personal computer (PC), tablets, or smartphones) given its built-in Wi-Fi connectivity. This system was examined for the detection of SARS-CoV-2 nucleocapsid (N)-protein antigens in spiked nasopharyngeal (NP) swab samples and its performance was compared to a commercial potentiostat. The dual parallel biosensing of N-protein in this work was used as a self-validation of the biosensor. The combined BiSense and N-protein biosensor was finally examined for rapid diagnosis of COVID-19 patients and quantitative measurement of their viral loads. This custom-designed BiSense reader is crucial hardware and interface component of the internet-of-things technology which can be used for addressing the clinical needs of early, remotely, and accurate SARS-CoV-2 detection and adapted for electrochemical POCT of various protein biomarkers.

2. Results and discussion

The electrochemical POCT system developed in this work contains a dual N-protein immuno-biosensor and the BiSense bi-potentiostat (Scheme 1). In short, the dual N-protein inmmuno-biosensor used in this study consists of two WEs both immobilized with the monoclonal N-protein antibody. The justification for this dual detection is the need and relevance to the self-validation of POCT protein biosensing. The electrode strips were prepared in-house with the same dimension as the commercially available screen-printed electrodes (7 mm by 29 mm, with the working electrodes with a surface area of 2.8 mm^2 (1.4 mm by 2 mm)), designed in small size to reduce the volume of expensive drop-casted reagents (antibodies here). A numerical analysis was conducted to optimize the relative position of WEs, ensuring an acceptable distribution of the electrical current and voltage on both WEs in different steps of biosensing. The immuno-biosensor was accompanied by a custom-made and compact bi-potentiostat (BiSense) for conducting EIS measurements from the N-protein biosensors. BiSense can measure the impedance change associated with the immunoreaction of the N-protein analyte and the immobilized capture antibody on the electrode surface. The readout system is portable with a dimension of 18 cm × 15 cm × 9 cm (length in width in height), and lightweight (~500 g). The total cost of the reader is less than USD $40 and the strip cost does not exceed $2 per strip. This detection system offers all major characteristics required for near-patient use in clinical and remote settings.

2.1. Numerical modeling of the electrical functionality of the dual-electrode design

The finite element analysis of the electrical performance of the strips, based on the specific design of electrodes, was conducted using a two-dimensional (2D) numerical simulation in COMSOL in the presence of an electrolyte solution over the electrodes. The relative positions of WEs were numerically compared for different design configurations via examining the WEs' performance in terms of the acceptable current distribution and possible generation of noise signals. To this end, three different relative distances of WEs were examined, named distance small (DS), distance medium (DM), and distance large (DL) with the distances

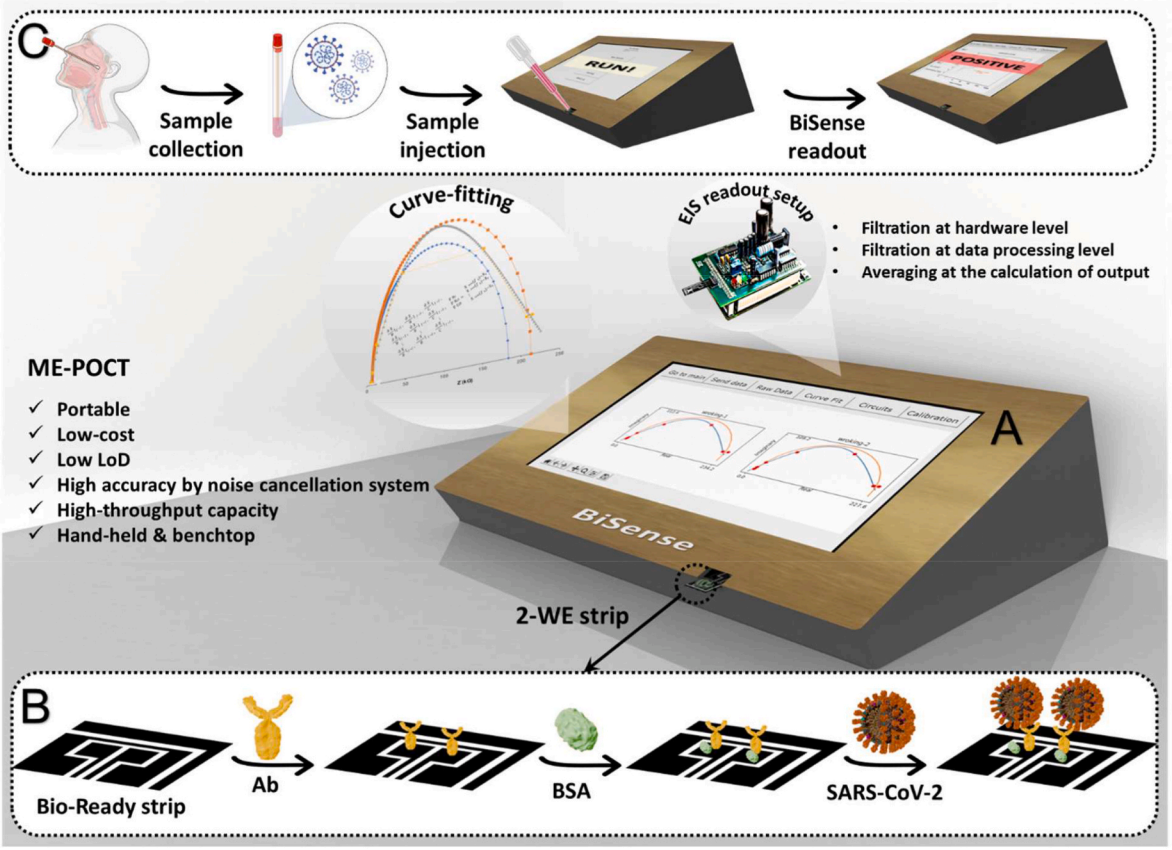

Scheme 1. Schematic representation of the (**A**) binary-sensing (BiSense) platform integrated with an immuno-biosensing detection unit, the multiplexed electrochemical point-of-care (ME-POCT) operational working principle, and specifications including the embedded readout set-up, and the curve-fitting algorithms for accurate data interpretation. The detection occurs via a (**B**) two-working electrode strip with the ready-to-immobilize carboxyl-rich surface for direct immobilization of antibodies (Ab), followed by blocking the surface using bovine serum albumin (BSA), for ultimate conjugation with the SARS-CoV-2 virus in clinical samples. (**C**) Following the nasopharyngeal (NP) swab specimen collection into the universal transport medium (UTM), one droplet of the sample is dropped cast on the strip to initiate the sensing process. Once the incubation of the sample is complete and the washing and redox probe delivery steps are performed, the BiSense bi-potentiostat reads the electrical signals from the two-working electrode (2WE) biosensing strips upon starting the process using the "Run" button, and it returns the results in less than 1.5 min.

of 125 μm, 300 μm, and 750 μm, respectively, and discretized with the generated mesh (Figs. S1A and B). The simulations were performed to characterize the electrical potential distribution and current streamlines across the reference electrode (RE), counter electrode (CE), and WEs, upon applying pre-defined electrical potentials to WEs.

Also, the electrolyte potential distribution was simulated at the areas between the electrodes (illustrated by surface plot representations) for all three design configurations (Fig. S1C). The results show that the potential distribution is strong (170 mV) near each of WE1 and WE2 and steadily diminishes toward zero at the CE. The potential distribution heatmaps are symmetric in the region around the WEs Fig. S1C), and the electrolyte current streamline vectors are parallel to the boundaries of the RE, indicating that no current flows through the insulated edges of the RE interface, as opposed to edges of the WEs and CE where the vectors are perpendicular to the domain boundaries (Fig. 1A (a-c). In addition to the symmetric design of the strip, in terms of the position of each of the electrodes, the current vectors are symmetric around the WEs which shows that the design exerts similar electrical conditions to each of the WEs, confirming the similarity of the signals collected from this dual-electrode system, a specification that adds to its reliable signal generation.

To evaluate the effect of distance between the WEs, the electrical current density of the electrolyte was plotted and the symmetric response of the two WEs was examined. Throughout the cut line (highlighted in Figure S1A), the output electrical current density decreases from 120 A/m2 to 69 A/m2 and 43 A/m2 in the area between the WE and CE. For all three designs, this current density is zero between the two WEs (Fig. S1D). Therefore, the output electrical current, as a measure of the current between the WE and CE, is attributed to the electrochemical properties of the surface and increases with increasing the distance between the two WEs. According to Fig. 1A and S1C, the plots of electrical current and potential together show that in the DL design, with increasing the horizontal distance between the two WEs (750 μm, Fig. 1A,a), a gradual potential difference is generated in the area between the two WEs, resulting in an unnecessary current flow in this area and a risk of noise generation. For the DL design with 125 μm distance between the WEs, it was observed that the upper and lower edges of the WEs allow for a higher current flow to the CE compared to the side edges (Fig. 1A,c), which is not desirable given that it generates inconsistencies in the electrical current of the side edges and the top edge. To ascertain that all areas of the WEs are involved equally in the sensitive signal generation, it is desirable to have a uniform current flow throughout all edges, as observed in the DM design (300 μm distance between the WEs, Fig. 1A and b). The numerical simulation verifies that with a constant potential difference between the WEs and the CE, the relative distance between the WEs plays an important role in the electrical current distribution, affecting the sensitivity of the electrodes. Hence, through the numerical analysis, it was shown that the DM design presents the optimal function in terms of uniformity of the current flow and potential around the WEs and therefore selected for further fabrication and testing.

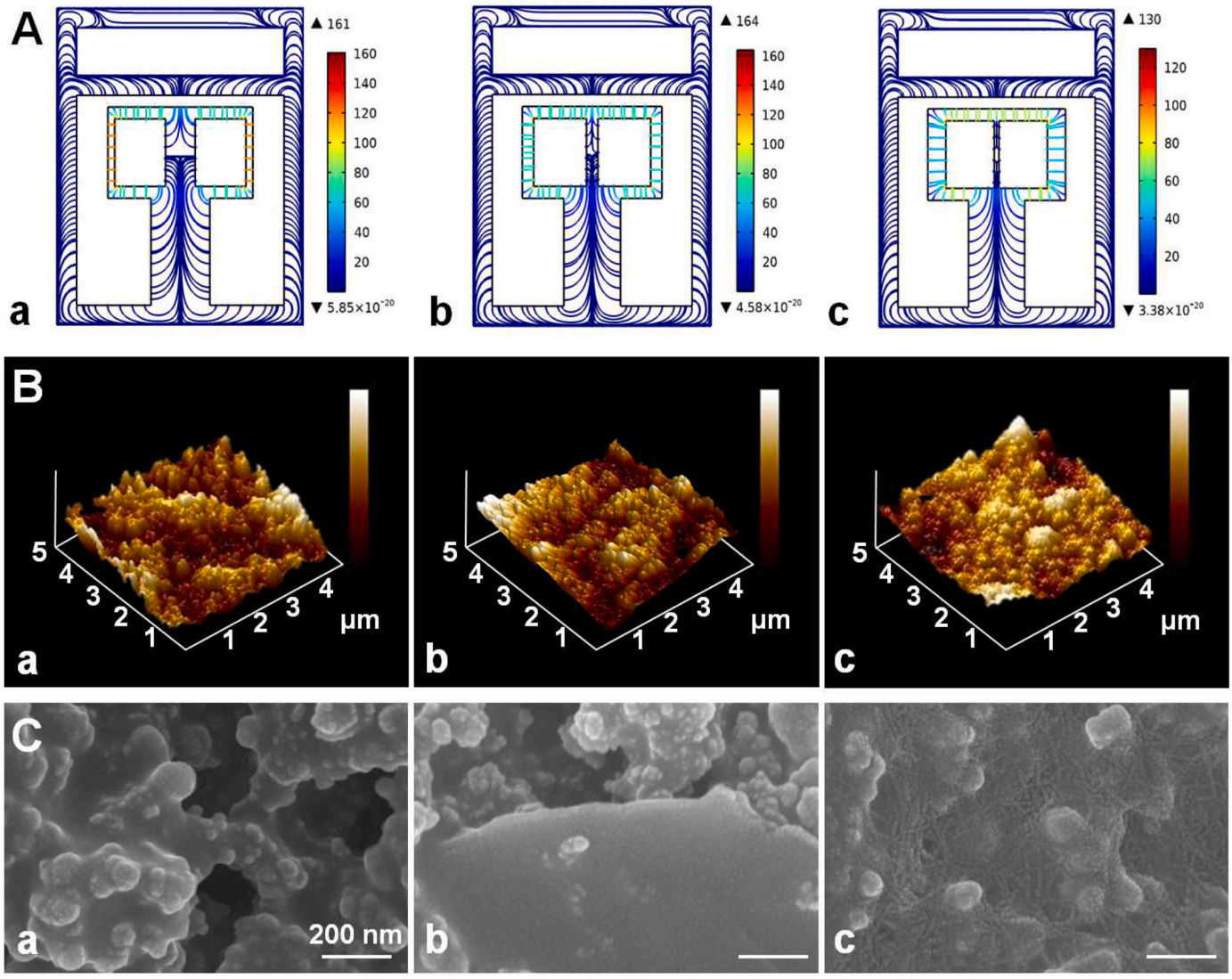

Fig. 1. Numerical electrochemical analysis and physical characterization of the intermixed Carbon PEDOT:PSS Graphene (iCPG) electrodes. (**A**) Numerical analysis of the electrical performance of the sensing strips using COMSOL simulations for three different electrode designs of a) distance large (DL), b) distance medium (DM) and c) distance small (DS), with a distance of 750 µm, 300 µm, and 125 µm between the two working electrodes, respectively. Topographical representation using **(B)** atomic force microscopy (AFM) and **(C)** field emission scanning electron microscopy (FESEM) imaging of a) the strip printed with pure carbon ink, b) iCPG electrode containing the graphene nanosheets, and c) the antibody conjugated iCPG strip, respectively.

2.2. Characterization of the electrode's surface

The topography and roughness of the electrodes' surface, with hills and valleys, represent the increased surface area created in the screen printing of the intermixed Carbon PEDOT:PSS Graphene (iCPG) nanocomposite ink. To characterize the electrode surface, the electrodes were examined by atomic force microscopy (AFM) tapping mode. The extracted data on the root-mean-square (RMS) roughness of the electrode surface (measured by R_q) shows that the incorporation of nanostructures to the base carbon ink increases the roughness of the surface, perceived through an increase in the RMS value changing from 82 nm for the base carbon ink to 115 nm for the nanocomposite ink. Furthermore, antibody immobilization on the electrode resulted in the formation of a smoother surface as these proteins fill the valleys of the surface, decreasing the RMS down to 88 nm. The 3D images of the AFM confirm the surface transitions during the antibody immobilization step (Fig. 1B). It is noted that the iCPG ink composition has carboxyl functionalized groups, therefore the antibodies are immobilized on the electrode without any need for common functionalization steps, as we previously demonstrated in our previous work (Salahandish et al., 2022a).

The electrode surface was further characterized using field emission scanning electron microscopy (FESEM) to assess the existence of graphene sheets in the inter-mixed nanocomposite ink and the antibodies on the iCPG printed ink. The FESEM images were acquired for three distinct surfaces, including the pure carbon bare electrode (Fig. 1C,a), the iCPG electrode (Fig. 1C,b), and the antibody-coated iCPG (Fig. 1C,c). The surface morphology of printed pure carbon electrode (Fig. 1C,a) confirms the presence of holes and projections, resulting in an enhanced surface area while the graphene nanosheets are detectable in the hybrid iCPG ink, feasibly trackable in the FESEM image (Fig. 1C,b). Following the antibody immobilization, the holes of the electrode surface are filled with antibodies where the coating is vividly observable in form of strands due to the preparation of the antibody solution in salty phosphate-buffered saline (PBS) (Fig. 1C,c). Furthermore, the uniformity of both printed carbon and iCPG inks on the electrodes was assessed by measuring the sheet resistance in different spots of the printed electrode with a 1 mm distance between each of the two probes.

The resistivity data were extracted for both bare carbon and bare iCPG electrodes (SI–B). The results show that the addition of the ink decreased the conductivity of the electrode surface from 1602.60 ± 26.35 for the bare carbon electrode to 1028.99 ± 34.71 for the nanocomposite ink electrode (RSD of 1.64% and 3.37%, respectively). The small RSD of the nanocomposite ink printed electrode confirms the uniform printing of this ink, verifying that the resistance change observed in electrochemical detection of target proteins would be dominantly attributed to the protein concentration and not the inconsistency in electrodes.

2.3. Rapid and reliable data reading from BiSense

BiSense enables the measurement of impedance with an accuracy comparable with the other standard electrochemical spectroscopy systems. As shown in the supplementary (SI–F to SI-J, Figs. S9–S14, and Tables S3 and S4), this custom-made palm-size light BiSense potentiostat device with less than 1% cost of the portable impedance spectroscopy systems offers a great advantage of a low-cost readout system for mass production during the situations like COVID-19 pandemic or the use as a point-of-care device in low-income countries.

Among all electrochemical sensing techniques, the EIS method has gained enormous popularity (Abdullah et al., 2019; Magar et al., 2021; Srivastava et al., 2018), owing to its high sensitivity in detecting a very low concentration of analytes and its flexibility in utilizing the Faradaic mode of detection for observing the variation in charge transfer resistance (R_{ct}). The custom-made BiSense bipotentiostat developed in this study is designed for reading the EIS signals from two WEs simultaneously. In the EIS method, there exists a potential frequency range through which the signal generation is performed, and data sampling occurs in defined frequency values based on the number of frequency scan (sampling) points. The fewer the number of sampling points is, the faster the readout step is performed, although typically a number of 50 sampling points is used for accurate biosensing applications. Here, BiSense uses the least square curve-fitting approach to reliably extract R_{ct} using a lower number of frequency points (seven different frequency points for each WE) which is beneficial in developing a faster reader.

The functionality of BiSense in generating EIS signals was compared to the EIS signals collected from the Autolab Potentiostat/Galvanostat equipped with a frequency response analysis (FRA) module with the performance tested under the same experimental conditions. Different concentrations of $[Fe(CN)_6]^{3-/4-}$ redox probe (ranging from 1 mM to 5 mM) were prepared in 1X PBS and utilized for conducting the EIS measurements from the 2-WE iCPG electrodes, where both WEs were treated identically to minimize the potential deviations as a result of the variation in WEs. The EIS measurements were carried out using seven frequency sampling points, ranging from 1400 Hz to 1 Hz, assigned to the settings of both homemade and commercialized potentiostat systems. The modified strips showed a justifiable signal in both WEs, as proven by a logical correlation of $R^2 = 0.98$ between the redox concentrations and R_{ct} values measured using BiSense (Fig. 2A). The correlation values of R_{ct} between BiSense and the Autolab potentiostat (both reading seven frequency points) extracted from WE1 and WE2 were measured to be 0.97 and 0.98, respectively (Fig. 2B). Also, the correlation value of R_{ct} between BiSense (seven frequency points) and the Autolab (50 frequency points) set with the same frequency range was measured to be 0.97 (Fig. 2C). The results show that the number of frequency points selected by the Autolab potentiostat has a negligible effect on the extracted signal where R_{ct} is < 180 kΩ. The only difference

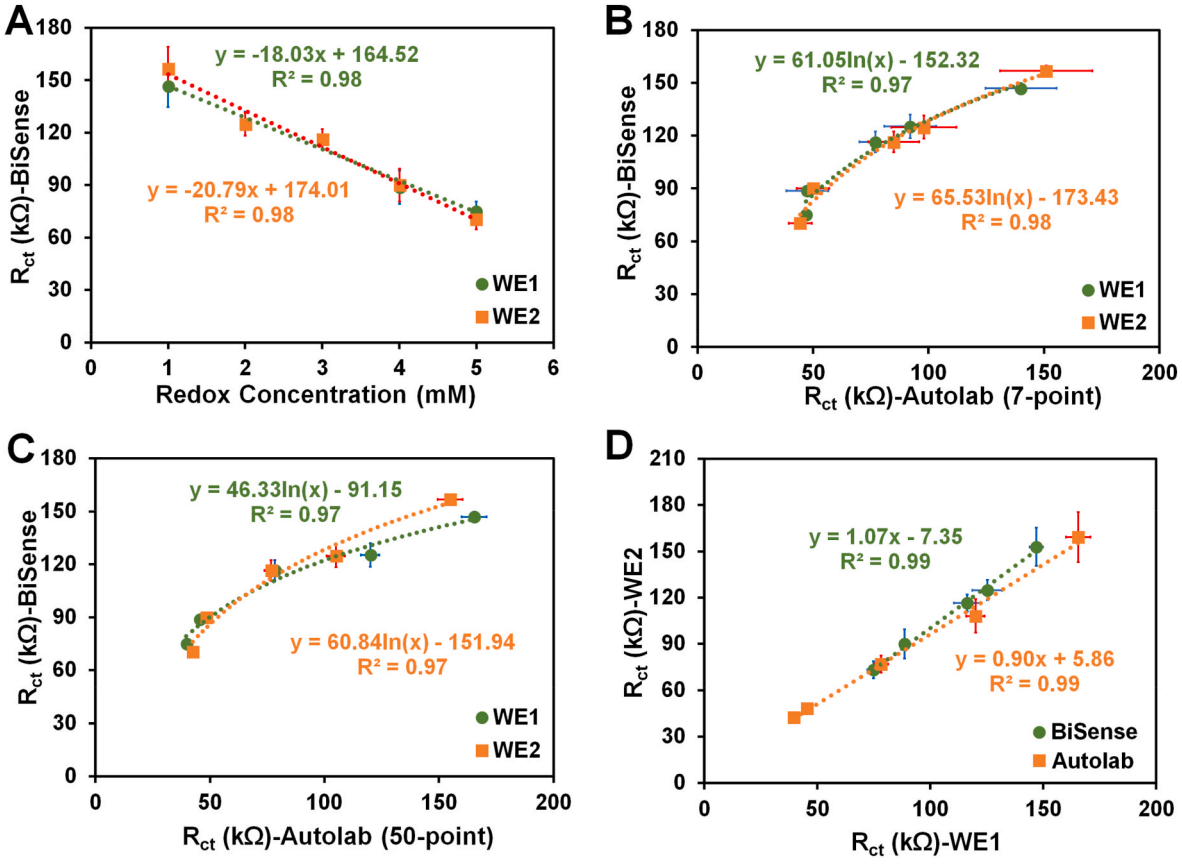

Fig. 2. The BiSense electrochemical potentiostat was compared to the commercial Autolab potentiostat for measuring EIS signals of both working electrodes (WE1 and WE2) in the presence of different concentrations of $[Fe(CN)_6]^{3-/4-}$ redox probe (1, 2, 3, 4, and 5 mM). **(A)** EIS Measurements performed using BiSense. **(B)** and **(C)** Comparing the measurements performed using BiSense against Autolab potentiostat with seven frequency points and 50 frequency points, respectively. **(D)** Correlative analysis of WE1 and WE2 signals measured by BiSense and the Autolab potentiostat.

observed was the average value of standard deviation (SD), considering both WEs responses in all concentrations of the redox probe, which increases from 4.84 to 10.11 in seven frequency point mode as opposed to 50 frequency point mode.

The comparative performance of WE1 and WE2 using both BiSense and the Autolab system at different concentrations of the redox probe (1, 2, 3, 4, and 5 mM) shows a linear correlation with the slope of 1.07 and 0.90 for BiSense and Autolab potentiostat, respectively (Fig. 2D). The R_{ct} values obtained from WE1 and WE2 are closer to each other when measured by the BiSense reader than the Autolab reader. The average error in the EIS signals measured for all redox probe concentrations between the two WEs was calculated to be 1.8% for BiSense and 4.47% for the Autolab potentiostat (Fig. S2). This may be attributed to the fact that the BiSense signals are recorded simultaneously from both WEs while the Autolab reader acquires the signal from WE2 following the completion of the signal reading from WE1.

2.4. Comparative biosensing analysis of BiSense and a commercial Autolab potentiostat

The functionality of the Autolab potentiostat and homemade BiSense potentiostat during the preparation steps of the immuno-biosensor and quantification of the N-protein antigens in spiked samples was further assessed. A significant increase in R_{ct} following each step of surface modification, from the iGCP electrode to the antibody-immobilized strips and bovine serum albumin (BSA) coated electrodes, depicts a logical response of the Autolab potentiostat and Bi-Sense. The Autolab potentiostat was set to acquire the EIS data based on seven frequency scan points (Fig. 3A,a and b, and Fig. S3A). The data obtained for the bare iCPG electrodes shows $R_{ct} = 40.79 \pm 2.02$ for WE1 and $R_{ct} = 49.28 \pm 1.75$ for WE2 in the presence of 2.5 mM redox probe (Fig. S3A). For the antibody-immobilized electrodes, the R_{ct} increased to 93.69 ± 7.10 and 96.32 ± 7.30 for WE1 and WE2, respectively. For the BSA-coated and antibody-immobilized electrodes (coating with 0.005% (w/v) BSA concentration), the R_{ct} increased to 330.89 ± 106.88 and 301.44 ± 114.59 for WE1 and WE2, respectively.

Furthermore, different concentrations of SARS-CoV-2 N-protein, ranging from 1 pg/mL to 10,000 pg/mL, were incubated on the N-protein immuno-biosensor. Briefly, the N-protein immuno-biosensor was prepared by adding the monoclonal N-protein antibody to the surface of iGPC electrodes followed by coating the antibody-immobilized surface with the blocking BSA solution to prevent any non-specific binding (details provided in Materials and Methods). The incubation on the immuno-biosensor with the N-protein spiked samples was followed by the washing and redox probe delivery steps, prior to reading the EIS signals using the Autolab potentiostat. The measured EIS signals were used to obtain the corresponding calibration curve of the N-protein biosensor, correlating different concentrations of the N-protein antigen spiked in PBS and the R_{ct} values obtained from the Nyquist plots. To assess the sensitivity and limit of detection (LoD) of the immuno-biosensor, antigen spiked samples were prepared in concentrations of 1, 10, 100, 1000, and 10,000 pg/mL, and drop-casted on the immobilized and passivated electrodes (Fig. 3A,a and b). The results of EIS signal show an increase in R_{ct} values in response to the increase in N-protein concentration. The calibration curve of the N-protein immuno-biosensor for detecting N-protein antigens in the spiked samples was fitted through the data points of R_{ct} signals, showing a logarithmic correlation $y = 30.51 \ln(x) + 520.43$, $R^2 = 0.68$ for WE1 and $y = 36.83 \ln(x) + 474.40$, $R^2 = 0.84$ for WE2.

The previous set of measurements was repeated with 50 frequency scan sampling points using the Autolab system to assess the possible deviations from the data of seven frequency scan points in terms of the curve fitting and R_{ct} values (Fig. 3B,a and b, and Fig. S3B). The results of measurement with the Autolab potentiostat also show the increase in R_{ct} values with the increase in N-protein concentrations in the spiked samples. When testing the dual immuno-biosensor with the Autolab potentiostat under the testing with seven frequency scan points, the concentration of N-protein was correlated with the R_{ct} signals based on the logarithmic equations of $y = 28.60 \ln(x) + 520.91$ for WE1 and $y = 31.78 \ln(x) + 476.71$ for WE2. Increasing the number of frequency

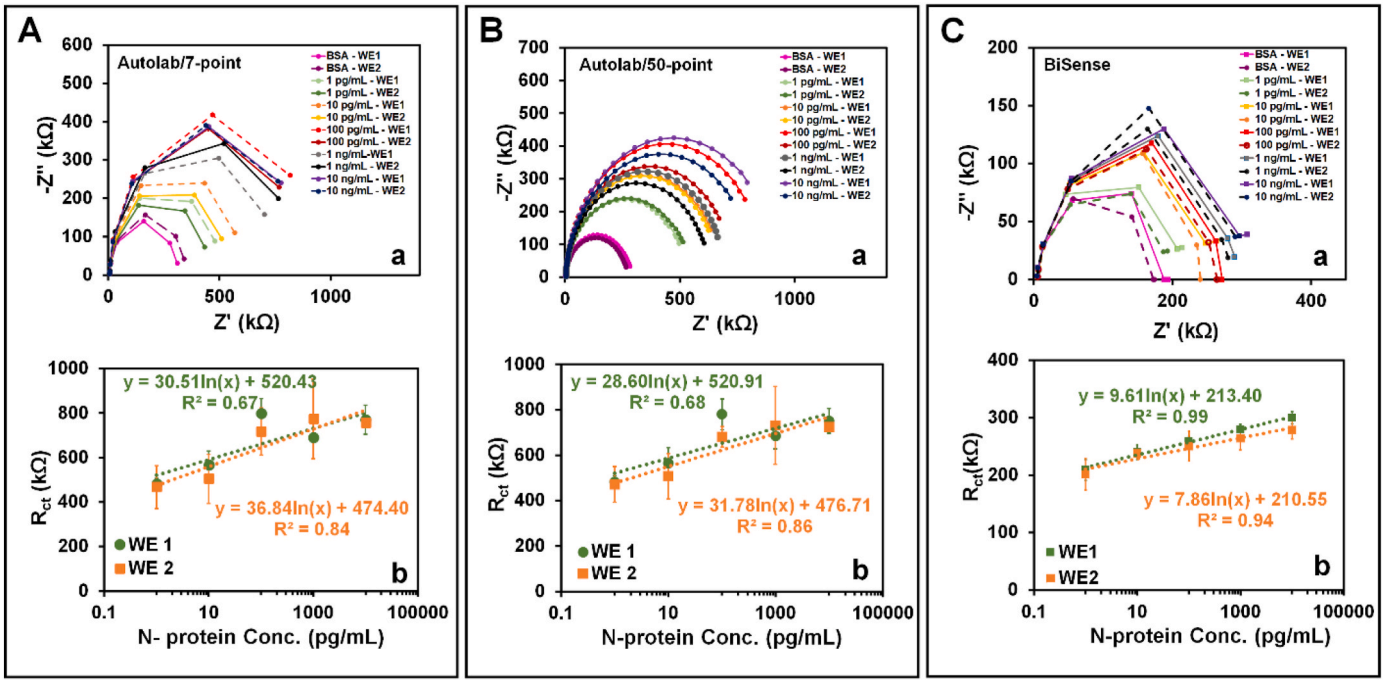

Fig. 3. Electrochemical characterization of the N-protein immuno-biosensor using an Autolab potentiostat and the BiSense reader. (**A**) Impedance response of the N-protein immuno-biosensor measured using the Autolab potentiostat in seven frequency sampling points. a) Nyquist plots associated with the impedance response of the immuno-biosensor tested with different concentrations of N-protein (1, 10, 100, 1000, and 10,000 pg/mL) spiked in phosphate buffer saline (PBS) and b) the corresponding calibration curves for both WEs. (**B**) Similar impedance response to (A) but the signals are measured using the Autolab potentiostat with 50 frequency sampling points. (**C**) Similar EIS signals measured in (A) and (B) but here measured with BiSense using seven frequency sampling points.

sampling points to 50 frequency scan points in the tests performed using the Autolab potentiostat resulted in a slight increase in R^2 from 0.67 to 0.68 for WE1 and 0.84 to 0.86 for WE2. The higher number of sampling points, the more accurate the curve fitting and an improved R_{ct} extraction, owing to the fact that the accuracy of curve fitting is dependent on scanned data points. Although higher precision is favorable, the data acquisition using 50 frequency scan points is much slower than the seven frequency scan points (approximately seven times slower in this study), which is a challenge for rapid testing.

The BiSense potentiostat was further examined for detecting N-protein in spiked samples under similar experimental conditions tested above with the Autolab potentiostat. The R_{ct} values were technically extracted from the Nyquist curve by fitting a curve on the acquired data points. The electrochemical system was represented with a fitted equivalent circuit, composed of electrical elements of resistance or Q (CPE: constant phase element) and capacitance. The Nyquist plots obtained using BiSense were fitted with R_s [R_{ct}C] circuit with a non-linear least-square fitting to measure all parameters from seven frequency scan points. All relevant information on the fitting process is presented in SI-D (Fig. S4, Table S2, and Eqs. S4 to S9).

For the BiSense potentiostat, the EIS signals were measured during the immuno-biosensor preparation steps, including antibody immobilization, BSA surface blocking, and immunoreaction with the spiked samples (Fig. 3C,a and b, and Fig. S3C). Following the immobilization of anti-N-protein on WEs, the R_{ct} values increased from 14.04 ± 1.19 kΩ for WE1 and 14.42 ± 1.80 kΩ for WE2, to 122.37 ± 3.57 kΩ for WE1 and 123.02 ± 3.50 kΩ for WE2. Following the BSA casting on the electrodes, the R_{ct} values increased to 171.25 ± 18.42 kΩ for WE1 and 169.16 ± 12.42 kΩ for WE2 (Fig. S3C). The biosensors were tested with different concentrations of N-protein spiked samples and corresponding R_{ct} values were measured using BiSense. The data was used to obtain the calibration curve of the N-protein immuno-biosensor, showing the capability of the biosensor/BiSense unit in detecting spiked N-proteins within a wide detection range of 1 pg/mL to 10,000 pg/mL. This calibration curve is presented with a logarithmic equation $y = 9.61 \ln(x) + 213.40$ ($R^2 = 0.99$) for WE1 and $y = 7.85 \ln(x) + 210.55$ ($R^2 = 0.94$) for WE2, demonstrating a significant increase in the correlation coefficient which confirms the reliability of the BiSense potentiostat. The LoD of the immuno-biosensor with the signals measured using BiSense was calculated for each of WEs based on LoD = 3S/N, where LoD of WE1 and WE2 are determined to be 56 fg/mL and 68 fg/mL, respectively. The results show the reliability of BiSense compared to the commercialized Autolab potentiostat, with a wider detection range and higher R^2 values while only using seven frequency scan points.

The BiSEnse readout system was developed to perform only 7 point sampling scan to reduce the signal reading period down to 90 s. Therefore, while the strip assay time is about 10 min, the signal reading last less than 90 s for reading both WEs, which provides an opportunity for improved throughput performance of this reader in the future planned studies. For example, one reader can read the signals of 5 strips (each strip with two WEs) in less than 12 min (~25 tests/hr/reader).

A comparative analysis between BiSense and the Autolab potentiostat was performed for biosensing of different concentrations of N-protein antigens in the presence of a 2.5 mM redox probe. The average error in R_{ct} values obtained for all concentrations of the antigen detected on the dual biosensor was less than 3.6% for BiSense and 7.12% for the Autolab potentiostat (Fig. S5). This comparative analysis verifies that the EIS signals need to be collected simultaneously from the two WEs (or any other multiplexing biosensors) for detecting either the redox or the target antigen concentrations. The calibration curves for the measurements conducted using Autolab are not reliable due to the low R^2 value, and the large error bars depict a high deviation of data, two shortcomings successfully resolved using BiSense. It is worth noting that the antifouling characteristics of the surface of the strips and the low complexity of the UTM media enabled the detection of N-proteins using both working electrodes without any need for using one of them for eliminating matrix effects. Fig. S6 shows that there isn't any significant difference between the signals obtained for UTM coated electrodes and PBS coated ones, both incubated for 30 min on BSA-deposited strips.

2.5. Clinical performance of BiSense and the immuno-biosensor for detecting COVID-19 patients

The BiSense reader in conjunction with the N-protein immuno-biosensor was employed for testing 22 clinical nasopharyngeal (NP) swab samples, containing 12 real-time reverse transcription-polymerase chain reaction (RT-PCR) confirmed alpha (B.1.1.7) variant SARS-CoV-2 infected patients and 10 negative NP swab samples (Fig. 4A). The EIS measurements were conducted using BiSense with seven frequency scan points collected. For SARS-CoV-2 positive samples with the cycle threshold (Ct) values reported to be between 19 and 31.5, the BiSense's EIS response show $R_{ct} >$ 194.89 kΩ (cut-off value), which is used to differentiate SARAS-CoV-2 positive samples from negative samples (with R_{ct} within the range of 147.42–178.97 kΩ). Each clinical sample was tested three times without any need for sample preparation. The repeatability of the measurements was acceptable with an average RSD of 10% (Fig. 4A) which is partially attributed to the non-homogeneous NP swab samples collected. There existed a significant difference (around 140 kΩ) between the negative and positive sample signals with an average of 312.10 ± 34.25 kΩ and 309.39 ± 23.67 kΩ for WE1 and WE2, respectively, for positive samples, and 171.24 ± 10.96 kΩ and 169.17 ± 10.94 kΩ, for WE1 and WE2, respectively, for negative samples. BiSense not only successfully differentiated positive patients and negative samples comparable to RT-PCR, it provided the quantitative concentration of N-proteins representing the viral loads, with a much lower reagent and sample consumption needed for RT-PCR. This quantitative measurement of viral loads is an advantage of quantitative electrochemical biosensors as opposed to the qualitative commercial colorimetric N-protein assays (e.g., Abbott PanBio rapid antigen kits). Using the Abbott Panbio Rapid Antigen COVID tests as lateral flow assay-based kits, we also confirmed that all of the 22 PCR-negative or positive samples used in this study were distinguishable, as a validation for the results obtained using BiSense.

The selective response of the N-protein immuno-biosensor measured with BiSense was assessed by testing the clinical samples containing Influenza A (Ful A) and B (Flu B) viral particles (Fig. 4B). While the R_{ct} values measured from SARS-CoV-2 positive samples is measured to be 261.82 ± 3.20 kΩ, the R_{ct} values for Flu A and B positive samples were measured to be 167.57 ± 8.74 and 176.77 ± 2.44 kΩ, respectively, an insignificant difference from the R_{ct} of the control sample. Also, the R_{ct} value of a mixed clinical sample containing SARS-CoV2, Flu A, and Flu B viruses (prepared using a mixing of three clinical samples, each positive to one of the viruses) tested on the N-protein biosensor was shown to have an insignificant difference to the R_{ct} measured from the corresponding SARS-CoV-2 positive sample, further confirming the selective response of the electrochemical POCT. The stable composition of the bioanalytes on the surface of the strips was assessed by acquiring the EIS signals of the immunosensors incubated with control nasopharyngeal samples for 3–5 h following the assay opening at room temperature. The associated data represented in Fig. S7 shows that no significant signal change was detected throughout this time window.

2.6. Software development and automating the function of the BiSense potentiostat

To improve the user experience working with BiSense and its features, the customized EIS board was integrated with a low-power Linux-based single-board computer (SBC). A user-friendly python-based graphical user interface (GUI) was developed to automate data collection, storage, and analysis. The integrated device contains the EIS board, a 7-inch liquid crystal display (LCD), and an affordable SBC Raspberry Pi 4 containing the Wi-Fi module. The potentiostat is also connected to the

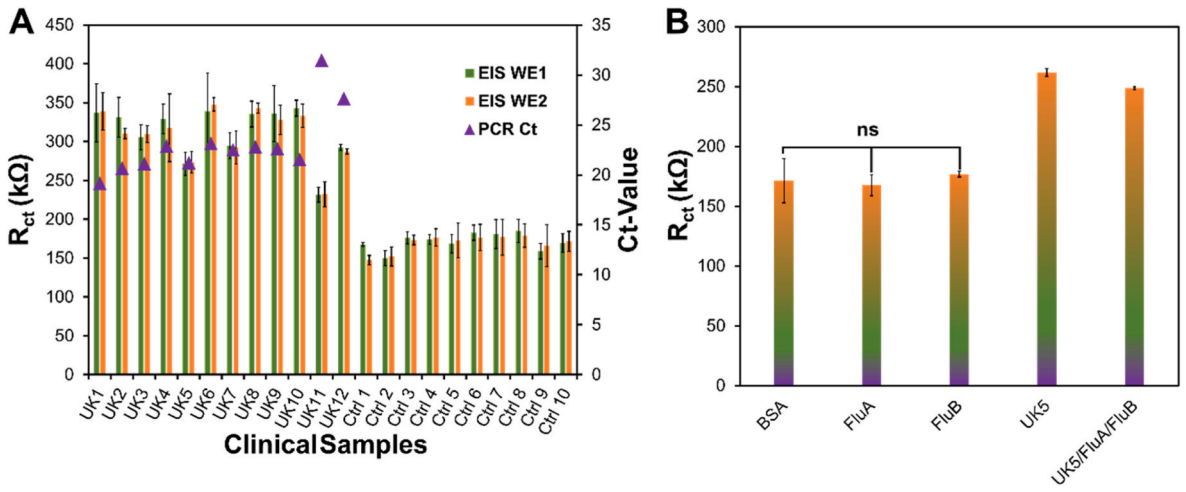

Fig. 4. The performance of BiSense in (**A**) detecting alpha (B.1.1.7) variant SARS-CoV-2 infected patients and differentiating them from negative control subjects (negative to SARS-CoV-2). The R_{ct} values are compared to Ct values quantified with real-time quantitative reverse transcription-polymerase chain reaction (RT-PCR), (**B**) the selectivity assessment of the immuno-biosensor/BiSense in detecting SARS-CoV-2 positive samples. The difference in the signal of the Influenza A (Flu A) and Influenza B (Flu B) with the BSA as a blank is non-significant (ns).

internet to store and analyze the raw data on the Cloud database (accessible at the University of Calgary) for further data processing. To preserve the printed circuit board (PCB) from contamination with clinical samples, a three-dimensional (3D) printed case was printed and housed BiSense and the interconnected compartments (Fig. S8).

As depicted in Video S1, following the switching on the BiSense device, the user is inquired to log in with a predefined ID, used to assign the saved data to the user. In the main menu, the 'New Sample' run triggers the data collecting functionality followed by inquiring for 'sample number', while the locally saved data are shown in 'Saved Data'. The other configurations such as Wi-Fi connection could be managed using the 'Configuration' setting. Following the collection of data from BiSense, the analysis of 'Raw Data' is run on the backend to fit the curve on the data points of the Nyquist plot. The non-linear least square curve fitting is performed to calculate R_{ct}, solution resistance (R_s), and double-layer capacitance (C_{dl}). The 'Curve Fit' frame shows the Nyquist plot while the 'Circuits' frame presents the extracted R_{ct}, R_s, and C_{dl}. Ultimately, the 'Calibration' frame shows the calibrated curve, used to measure the antigen concentration based on the returned R_{ct} value. The axes of the Nyquist plot are defined as Imaginary ($-Z''$) versus Real (Z') in kΩ, then fitted with the semicircle with the diameter R_{ct} and a high-frequency intercept on the real axis R_s. A basic toolbox was designed in this frame to extract extra information of the data points and the fitted curve. The NumPy and matplotlib libraries in python were utilized to implement the mathematical model and the curve-fitting algorithm.

Supplementary video related to this article can be found at https://doi.org/10.1016/j.bios.2022.114459

3. Conclusion

There is a crucial need for accessibility to accurate, reliable, low-cost, and handheld potentiostat readers compatible with multiplex electrochemical biosensors while it is adaptable to point-of-care applications. This work presents a new bi-potentiostat reader (BiSense) for simultaneous impedance signal acquisition from an immunoaffinity-based dual-working-electrode strip. The electrochemical immuno-biosensing strip was prepared with immobilization of N-protein antibody on homemade ready-to-sense conductive electrodes while it is compatible with the custom-designed BiSense reader. BiSense while is 100 times cheaper than the commercialized Autolab potentiostat, proved to outperform the Autolab potentiostat for the sensitive detection of N-protein and rapid signal reading (<1.5 min for reading the signals of both WEs, where using low-frequency sampling mode). The Nyquist curve fitting and R_{ct} calculations were automated using an integrated computing unit, offering rapid signal-to-result processing. This bi-potentiostat once combined with the ultrasensitive N-protein biosensor offers a very low limit of detections of 56 fg/mL for WE1 and 68 fg/mL for WE2 for the detection of SARS-CoV-2 N-protein in PBS samples. It also demonstrated its utility for differentiating COVID-19 infected patients from controls in less than 15 min, presenting its potency for early diagnosis of COVID-19 infected patients. This bi-potentiostat is compact, low cost, and rapid response for multiplexed biosensing applications as opposed to bulky and expensive potentiostats. This diagnostic platform has improved accuracy and fewer implementation hurdles compared to many other POCT methods, and therefore it has the potential to fill the gap that has been present in this diagnostic field during the pandemic. Accurate, low-cost, and rapid diagnosis of SARS-CoV-2 remain to be crucial in the COVID-19-endemic world in multiple clinical settings, especially rural and remote settings. Also, the technology with its multiplexing potential has high flexibility to be adopted for the differentiation of SARS-CoV-2 from other viral and bacterial infections. It also opens avenues for rapid quantifications of several protein biomarkers associated with different diseases using a cheap and expedited manner.

4. Experimental section

4.1. Design and fabrication of the two working electrode strips

The dimensions used for the drawings of the electrodes and the lead distance were selected based on the commercially available connector (Molex, 0472861001) and the manufacturing constraints imposed by the screen-printing method. The technical drawings were created according to the conventional sensing strips in the market and using AutoCAD 2021 Version: R.47.0.0 for 2D drawings of the 2-WE system. The hybrid ink used for printing the electrodes was made through mixing (mechanical stirrer, 100 rpm) the Graphene@PEDOT:PSS ink (dispersed in dimethylformamide (DMF), Sigma, USA) and a base carbon ink (7102, Dupont, USA). The printing process was initiated utilizing a custom-designed polyester mesh fixed on the screen-printing machine, Micro Flatbed Printer (World Trade, Inc., USA), followed by curing the electrodes in an InfraRed machine (Natgraph Dryer, Natgraph Ltd, UK). To cover the conductive areas of electrodes except for the intended counter, reference, and working spots, a double-sided pressure-sensitive adhesive sheet (ARcare 90106NB, Adhesive Research Inc., USA) was laser-cut by Speedy 360 flex CO_2 laser engraver machine (Trotec, USA) and attached to the printed electrode for insulating the

undesired areas.

4.2. BiSense potentiostat as a hand-held and low-cost bi-potentiostat

Rapid and reliable EIS signal recording from a 2-WE stript system requires a noise-free, accurate, rapid, and low-cost bi-potentiostat with the capability of simultaneous recording of signals from both WEs. The core of BiSense is a microcontroller (MC) featuring high-resolution Analog to Digital (ADC) and digital to analog (DAC) devices for generating and recording sinewave voltage respectively (Figs. S10 and S11b). Furthermore, this MC is used to digitally tune the passive elements in the active low pass filter (LPF) and the operational amplifier (OPAMP)-based attenuator to generate small excitation sinewave in the analog front-end circuitry. This circuitry is also connected to the CE, RE, and WE1 or WE2 (Fig. S11a). This MC-based readout circuitry allows for impedance measurement at seven different frequencies of 1, 3, 11, 37, 125, 412, 1390 Hz. Based on these measurements, in the second MC, the charge transfer resistance is computed in the presence of the target analyte on the electrodes. The second MC also enables graphical user interface (GUI) and wifi data communication (Fig. S13). While this low-cost and handheld readout system uses off-the-shelf components and a custom-made PCB, it enables a high accuracy impedance measurement (see Fig. S14). In addition to the outperformed function of BiSense as opposed to the Autolab potentiostat for dual biosensing, the low-cost, parallel sensing, portable, and customized BiSense is estimated to be priced at around USD $40, which is very low-cost compared to a fully functional single-channel Autolab potentiostat unit (PGSTAT204) costing USD $4000–6000.

4.3. Preparation of the immuno-biosensor

To immobilize SARS-CoV-2 nucleocapsid antibody (HC2003, GenScript Inc.USA) on the WEs, 50 μg/mL solution of the antibody spiked in PBS (1X, Growcells, CA, USA, pH = 7.4) was prepared and cast-coated on each WE, incubated at room temperature for 1 h and then overnight at 4 °C, and then rinsed and dried. The antibody-immobilized WEs were passivated with 0.005% (w/v) bovine serum albumin (BSA) (prepared with PBS) (ChemCruz, sc-2323, USA) following the drop-casting of the BSA solution on both WEs. Finally, the electrodes were incubated at room temperature for 30 min and then washed with PBS for 30 s.

4.4. Testing the immuno-biosensor/BiSense unit with spiked and clinical samples

The electrochemical characterization experiments were first performed using spiked samples of SARS-CoV-2 protein (#Z03488, GenScript Inc.USA) with protein concentrations ranging from 1 pg/mL to 10,000 pg/mL spiked in PBS. The antigen-spiked samples were prepared using a serial dilution of the stock protein in PBS. The EIS signals were recorded using both BiSense and a commercial Autolab potentiostat, PGSTAT 204 Potentiostat/Galvanostat (Autolab models, Metrohm, USA). An open circuit potential (E_{ocp}) of 0.17 V and signal amplitude of 10 mA was used for EIS measurements. The measurements were performed in a frequency range of 1400 kHz to 1 Hz.

The nasopharyngeal (NP) swab samples were collected from and provided to this study by Alberta Precision Laboratories (Alberta, Canada). The samples were previously tested with RT-PCR. The samples positive to SARS-CoV-2 have a Ct $<$ 37 while the Ct value of zero is considered for SARS-CoV-2 negative samples since these samples are pre-pandemic collected specimens. Other control clinical samples contain influenza A and B positive samples. The clinical testing was performed in a specialized laboratory equipped with Class II Biosafety cabinet and according to the ethics # REB20-1032 and safety protocols confirmed by the University of Calgary. No prior lysing, heat-treatment, purification, or filtration was performed on the samples prior to testing them with the immuno-biosensors. The selective response of the N-protein biosensors and BiSense to SARS-CoV-2 was assessed by testing the biosensors with the clinical NP swab samples containing Influenza A or B viruses as well as the mixed virus clinical samples.

4.5. Characterization of the electrode surface

The atomic force microscopy (AFM, Bruker Nanoscope, Germany) in the tapping mode was utilized to investigate the topography of the electrode surface. The field emission scanning electron microscopy (FESEM, Sigma- ZEISS, Germany) micrographs were obtained by an electron beam sweep on the electrode surface to characterize the morphology of the nanostructures. All surfaces were pre-coated with gold to improve the SEM image resolution. The resistivity (or electrical conductivity) of different spots of the electrodes printed on polyethylene terephthalate (PET) sheets was measured using a multimeter (Keysight 34460 A) connected to a four-probe station.

4.6. Computational modeling of electrical current distribution on two-working electrode strip

To optimize the distance between the two WEs, the electrical current distribution and the potential difference between the electrolyte and each WE on the four-electrode strip design were computationally simulated in 2D using Primary Current Distribution Module in COMSOL Multiphysics 5.6. The geometrical domain of the system for numerical simulations was created using our previously introduced two-working electrode design with identifiable two WEs, one reference, and one counter electrodes (Fig. S1A).(Salahandish et al., 2022a) The numerical simulation was applied to three different electrode designs with different distances between the two WEs while having a similar distance of WEs to the counter and reference electrodes. The three different electrode designs with the distances between WEs set to 0.750, 0.300, and 0.125 mm (denoted DL, DM, and DS, respectively) were subject to computational modeling (Fig. S1A). The area between each of the electrodes is considered filled with the electrolyte in the numerical model to enable computational modeling of charged ion transport from a homogenous electrolyte to the electrodes. Ohm's law and balance of charges were also used to model the current conduction in the electrodes based on the applied potentials. The potentials of 170 and 0 mV were assigned to the working and counter electrodes, respectively. To estimate the potential difference between the surface-electrolyte and charge distribution at the electrode-electrolyte interface, a finer triangular mesh was used to simulate surface current density and electrolyte potential (Figure S1B). A non-Neumann boundary condition was used to apply electrical insulation to the reference electrode. It is noted that employing the screen-printing technique and the hybrid ink used in this study, the minimum feature size could not be less than 0.125 mm. The details of simulation conditions and the governing equations are discussed in SI-A.

The information on the numerical simulation equations and solution steps. Representations of the boundary conditions applied to the electrodes in the numerical analysis and associated potential distribution plot. The equations used for calculating the electrical resistivity and conductivity of the strips, along with a table representing the obtained data for these parameters. Error percentage for the measurements in electrochemical characterization between BiSense and the Autolab potentiostat using various concentrations of the redox solution. Nyquist plots of signals obtained using the Autolab potentiostat, both 7 and 50 points frequency scans, and BiSense for step-by-step surface modification with the antibody, BSA, and antigen. The governing equations and explanations of the Nyquist curve fitting process. Error percentage for the measurements comparing the BiSense and the Autolab potentiostat performance using various concentrations of the N-protein antigen. Immunosensor response to UTM media and PBS incubated on working electrodes for evaluating matrix effect. Immunosensor stability

assessment upon maintaining the antibody immobilized strips at room temperature. BiSense readout system functionality, operational procedure, governing principles of impedance-based data acquisition, the electrical circuitry design and noise cancelation system, printed circuit board (PCB) implementation, system costs, and the BiSense graphical user interface.

Author contributions

Concept and design: R.S, H.OT, E.GZ, A.SN; Experimentation & Data acquisition: R.S, P.J, H.OT, J.EH, F.H; Data analysis and/or interpretation: R.S, P.J, H.OT, E.GZ, A.SN; Numerical analysis: R.S, F.H, A.Z; Clinical sample analysis: R.S, J.EH, B.B, D.N; Drafting and revising the manuscript: R.S, F.H, P.J, H.OT, M.Kh, A.Z, B.B, D.N, E.GZ, A.SN.

Notes

The authors declare no competing interests.

Declaration of competing interest

The authors declare that they have no known competing financial interests or personal relationships that could have appeared to influence the work reported in this paper.

Acknowledgements

The authors acknowledge the Canadian Institutes of Health Research (CIHR) and Natural Sciences and Engineering Research of Canada (NSERC) for their Rapid COVID-19 Response fundings. The authors also acknowledge the Canada Research Chair, NSERC CREATE, Wearable Technology Research and Collaboration (We-TRAC) Training Program (Project No. CREATE/511166-2018), University of Calgary, and CMC – Microsystems, Canada for supporting this research. The authors would also like to thank the Alberta Public Health Laboratory in Calgary and their research staff members LeeAnn Turnbull and Kanti Pabbaraju for their support in providing access to clinical samples.

Appendix A. Supplementary data

Supplementary data to this article can be found online at https://doi.org/10.1016/j.bios.2022.114459.

References

Abdullah, S., Tonello, S., Borghetti, M., Sardini, E., Serpelloni, M., 2019. Potentiostats for protein biosensing: design considerations and analysis on measurement characteristics. J. Sens. 2019, 1–20.
Akhavan, O., Ghaderi, E., Rahighi, R., Abdolahad, M., 2014. Spongy graphene electrode in electrochemical detection of leukemia at single-cell levels. Carbon 79, 654–663.
Alam, A.U., Clyne, D., Jin, H., Hu, N.-X., Deen, M.J., 2020. Fully integrated, simple, and low-cost electrochemical sensor array for in situ water quality monitoring. ACS Sens. 5 (2), 412–422.
Alam, F., Hasan, M.M., Siddiquee, M.R., Forouzanfar, S., Jalal, A.H., Pala, N., 2021. Miniaturized, wireless multi-channel potentiostat platform for wearable sensing and monitoring applications. Smart Biomed. Physiol. Sensor Technol. XVIII, 117570H. International Society for Optics and Photonics).
Arduini, F., Micheli, L., Moscone, D., Palleschi, G., Piermarini, S., Ricci, F., Volpe, G., 2016. Electrochemical biosensors based on nanomodified screen-printed electrodes: recent applications in clinical analysis. TrAC, Trends Anal. Chem. 79, 114–126.
Bianchi, V., Boni, A., Bassoli, M., Giannetto, M., Fortunati, S., Careri, M., De Munari, I., 2021. IoT and biosensors: a smart portable potentiostat with advanced cloud-enabled features. IEEE Access 9, 141544–141554.
Bianchi, V., Boni, A., Fortunati, S., Giannetto, M., Careri, M., De Munari, I., 2019. A Wi-Fi cloud-based portable potentiostat for electrochemical biosensors. IEEE Trans. Instrum. Meas. 69 (6), 3232–3240.
Capaldo, P., Alfarano, S.R., Ianeselli, L., Zilio, S.D., Bosco, A., Parisse, P., Casalis, L., 2016. Circulating disease biomarker detection in complex matrices: real-time, in situ measurements of DNA/miRNA hybridization via electrochemical impedance spectroscopy. ACS Sens. 1 (8), 1003–1010.
Castle, L.M., Schuh, D.A., Reynolds, E.E., Furst, A.L., 2021. Electrochemical sensors to detect bacterial foodborne pathogens. ACS Sens. 6 (5), 1717–1730.
Chung, S., Sicklick, J.K., Ray, P., Hall, D.A., 2021. Development of a soluble KIT electrochemical aptasensor for cancer theranostics. ACS Sens. 6 (5), 1971–1979.
Clark, R.B., Glasscott, M.W., Verber, M.D., DeMartino, J.C., Netchaev, A., Ray, J.D., Brown, E.W., Alberts, E., Fernando, P.A.I., Moores, L.C., 2021. A generalized potentiostat adaptor for multiplexed electroanalysis. Anal. Chem. 93 (20), 7381–7387.
Dhanapala, L., Krause, C.E., Jones, A.L., Rusling, J.F., 2020. Printed electrodes in microfluidic arrays for cancer biomarker protein detection. Biosensors 10 (9), 115.
El Harrad, L., Bourais, I., Mohammadi, H., Amine, A., 2018. Recent advances in electrochemical biosensors based on enzyme inhibition for clinical and pharmaceutical applications. Sensors 18 (1), 164.
Gao, J., Jeffries, L., Mach, K.E., Craft, D.W., Thomas, N.J., Gau, V., Liao, J.C., Wong, P.K., 2017. A multiplex electrochemical biosensor for bloodstream infection diagnosis. Slas Technol.: Transl. Life Sci. Innovat. 22 (4), 466–474.
Haghayegh, F., Salahandish, R., Hassani, M., Sanati-Nezhad, A., 2022a. Highly stable buffer-based zinc oxide/reduced graphene oxide nanosurface chemistry for rapid immunosensing of SARS-CoV-2 antigens. ACS Appl. Mater. Interfaces 14 (8), 10844–10860.
Haghayegh, F., Salahandish, R., Zare, A., Khalghollah, M., Sanati-Nezhad, A., 2022b. Immuno-biosensor on a chip: a self-powered microfluidic-based electrochemical biosensing platform for point-of-care quantification of proteins. Lab Chip 22 (1), 108–120.
Hoilett, O.S., Walker, J.F., Balash, B.M., Jaras, N.J., Boppana, S., Linnes, J.C., 2020. KickStat: a coin-sized potentiostat for high-resolution electrochemical analysis. Sensors 20 (8), 2407.
Ibarlucea, B., Munoz-Berbel, X., Ortiz, P., Büttgenbach, S., Fernández-Sánchez, C., Llobera, A., 2016. Self-validating lab-on-a-chip for monitoring enzyme-catalyzed biological reactions. Sens. Actuators, B 237, 16–23.
Idili, A., Parolo, C., Alvarez-Diduk, R., Merkoçi, A., 2021. Rapid and efficient detection of the SARS-CoV-2 spike protein using an electrochemical aptamer-based sensor. ACS Sens. 6 (8), 3093–3101.
Khetani, S., Kollath, V.O., Eastick, E., Debert, C., Sen, A., Karan, K., Sanati-Nezhad, A., 2019. Single-step functionalization of poly-catecholamine nanofilms for ultra-sensitive immunosensing of ubiquitin carboxyl terminal hydrolase-L1 (UCHL-1) in spinal cord injury. Biosens. Bioelectron. 145, 111715.
Khetani, S., Ozhukil Kollath, V., Kundra, V., Nguyen, M.D., Debert, C., Sen, A., Karan, K., Sanati-Nezhad, A., 2018. Polyethylenimine modified graphene-oxide electrochemical immunosensor for the detection of glial fibrillary acidic protein in central nervous system injury. ACS Sens. 3 (4), 844–851.
Khetani, S., Singh, A., Besler, B., Butterworth, S., Lijnse, T., Loughery, K., Smith, K., Hosseini, E., Narang, R., Karan, K., 2021. μDrop: multi-analyte portable electrochemical-sensing device for blood-based detection of cleaved tau and neuron filament light in traumatic brain injury patients. Biosens. Bioelectron. 178, 113033.
Kinnamon, D.S., Krishnan, S., Brosler, S., Sun, E., Prasad, S., 2018. Screen printed graphene oxide textile biosensor for applications in inexpensive and wearable point-of-exposure detection of influenza for at-risk populations. J. Electrochem. Soc. 165 (8), B3084.
Liu, Z., Liu, J., Sun, T., Zeng, D., Yang, C., Wang, H., Yang, C., Guo, J., Wu, Q., Chen, H.-J., 2021. Integrated multiplex sensing bandage for in situ monitoring of early infected wounds. ACS Sens. 6 (8), 3112–3124.
Magar, H.S., Hassan, R.Y., Mulchandani, A., 2021. Electrochemical Impedance Spectroscopy (EIS): principles, construction, and biosensing applications. Sensors 21 (19), 6578.
Massey, T.L., Gleick, J.R., Razi–ul, M.H., 2021. Automated Multiplexed Potentiostat System (AMPS) for High-Throughput Characterization of Neural Interfaces. In: 2021 IEEE Biomedical Circuits and Systems Conference (BioCAS). IEEE, pp. 1–5.
Monošík, R., Stred'anský, M., Šturdík, E., 2012. Application of electrochemical biosensors in clinical diagnosis. J. Clin. Lab. Anal. 26 (1), 22–34.
Noah, N.M., Ndangili, P.M., 2019. Current trends of nanobiosensors for point-of-care diagnostics. J. Anal. Methods Chem. 12, 1–16.
Nyein, H.Y.Y., Tai, L.-C., Ngo, Q.P., Chao, M., Zhang, G.B., Gao, W., Bariya, M., Bullock, J., Kim, H., Fahad, H.M., 2018. A wearable microfluidic sensing patch for dynamic sweat secretion analysis. ACS Sens. 3 (5), 944–952.
Panes-Ruiz, L.A., Riemenschneider, L., Chawa, A., Moner, M., Loeffler, M., Rellinghaus, B., Tetzlaff, R., Bezugly, V., Ibarlucea, B., Cuniberti, G., 2021. Selective and self-validating breath-level detection of hydrogen sulfide in humid air by gold nanoparticle-functionalized nanotube arrays. Nano Res. 15 (3), 1–10.
Pansodtee, P., Selberg, J., Jia, M., Jafari, M., Dechiraju, H., Thomsen, T., Gomez, M., Rolandi, M., Teodorescu, M., 2021. The multi-channel potentiostat: development and evaluation of a scalable mini-potentiostat array for investigating electrochemical reaction mechanisms. PLoS One 16 (9), e0257167.
Park, S., Kwak, D.-e., Haque, A.-M.J., Lee, N.-S., Yoon, Y.H., Yang, H., 2022. Phenolic tyrosinase substrate with a formal potential lower than that of phenol to obtain a sensitive electrochemical immunosensor. ACS Sens. 7 (3), 790–796.
Pellitero, M.A., Curtis, S.D., Arroyo-Currás, N., 2021. Interrogation of electrochemical aptamer-based sensors via peak-to-peak separation in cyclic voltammetry improves the temporal stability and batch-to-batch variability in biological fluids. ACS Sens. 6 (3), 1199–1207.
Pimalai, D., Putnin, T., Waiwinya, W., Chotsuwan, C., Aroonyadet, N., Japrung, D., 2021. Development of electrochemical biosensors for simultaneous multiplex detection of microRNA for breast cancer screening. Microchim. Acta 188 (10), 1–10.
Pothipor, C., Jakmunee, J., Bamrungsap, S., Ounnunkad, K., 2021. An electrochemical biosensor for simultaneous detection of breast cancer clinically related microRNAs based on a gold nanoparticles/graphene quantum dots/graphene oxide film. Analyst 146 (12), 4000–4009.

Pruna, R., Palacio, F., Baraket, A., Zine, N., Streklas, A., Bausells, J., Errachid, A., López, M., 2018. A low-cost and miniaturized potentiostat for sensing of biomolecular species such as TNF-α by electrochemical impedance spectroscopy. Biosens. Bioelectron. 100, 533–540.

Ramfos, I., Vassiliadis, N., Blionas, S., Efstathiou, K., Fragoso, A., O'Sullivan, C.K., Birbas, A., 2013. A compact hybrid-multiplexed potentiostat for real-time electrochemical biosensing applications. Biosens. Bioelectron. 47, 482–489.

Salahandish, R., Haghayegh, F., Ayala-Charca, G., Hyun, J.E., Khalghollah, M., Zare, A., Far, B., Berenger, B.M., Niu, Y.D., Ghafar-Zadeh, E., 2022a. Bi-ECDAQ: an electrochemical dual-immuno-biosensor accompanied by a customized bi-potentiostat for clinical detection of SARS-CoV-2 Nucleocapsid proteins. Biosens. Bioelectron., 114018

Salahandish, R., Hassani, M., Zare, A., Haghayegh, F., Sanati-Nezhad, A., 2022b. Autonomous electrochemical biosensing of glial fibrillary acidic protein for point-of-care detection of central nervous system injuries. Lab Chip 22 (8), 1542–1555.

Salahandish, R., Zargartalebi, H., Janmaleki, M., Khetani, S., Azarmanesh, M., Ashani, M. M., Aburashed, R., Vatani, M., Ghaffarinejad, A., Sanati-Nezhad, A., 2019. Reproducible and scalable generation of multilayer nanocomposite constructs for ultrasensitive nanobiosensing. Adv. Mater. Technol. 4 (11), 1900478.

Srivastava, M., Nirala, N.R., Srivastava, S., Prakash, R., 2018. A comparative study of aptasensor vs immunosensor for label-free PSA cancer detection on GQDs-AuNRs modified screen-printed electrodes. Sci. Rep. 8 (1), 1–11.

Stradolini, F., Elboshra, T., Biscontini, A., De Micheli, G., Carrara, S., 2016. Simultaneous Monitoring of Anesthetics and Therapeutic Compounds with a Portable Multichannel Potentiostat. In: 2016 IEEE International Symposium on Circuits and Systems (ISCAS). IEEE, pp. 834–837.

Timilsina, S.S., Durr, N., Yafia, M., Sallum, H., Jolly, P., Ingber, D.E., 2021. Ultrarapid method for coating electrochemical sensors with antifouling conductive nanomaterials enables highly sensitive multiplexed detection in whole blood. Adv. Healthc. Mater., e2102244

Vinoth, R., Nakagawa, T., Mathiyarasu, J., Mohan, A.V., 2021. Fully printed wearable microfluidic devices for high-throughput sweat sampling and multiplexed electrochemical analysis. ACS Sens. 6 (3), 1174–1186.

Wu, D., Rios-Aguirre, D., Chounlakone, M., Camacho-Leon, S., Voldman, J., 2018. Sequentially multiplexed amperometry for electrochemical biosensors. Biosens. Bioelectron. 117, 522–529.

Zupančič, U., Jolly, P., Estrela, P., Moschou, D., Ingber, D.E., 2021. Electrochemical biosensors: graphene enabled low-noise surface chemistry for multiplexed sepsis biomarker detection in whole blood. Adv. Funct. Mater. 31 (16), 2170107.